Journal of Computational Physics 229 (2010) 7277–7286

Contents lists available at ScienceDirect

Journal of Computational Physics

journal homepage: www.elsevier.com/locate/jcp

About the ellipticity of the Chebyshev–Gauss–Radau discrete Laplacian with Neumann condition

B. Trouette *, C. Delcarte, G. Labrosse

Univ. Paris Sud 11, Limsi-CNRS, F-91405 Orsay, France

ARTICLE INFO

Article history:
Received 16 November 2009
Received in revised form 6 June 2010
Accepted 9 June 2010
Available online 16 June 2010

Keywords:
Polar Laplacian
Spectral collocation method
Ellipticity
Mapping

ABSTRACT

The Chebyshev–Gauss–Radau discrete version of the polar-diffusion operator, $\left(\frac{1}{r}\frac{\partial}{\partial r}\left(r\frac{\partial}{\partial r}\right)-\frac{k^2}{r^2}\right)$, k being the azimuthal wave number, presents complex conjugate eigenvalues, with negative real parts, when it is associated with a Neumann boundary condition imposed at $r = 1$. It is shown that this ellipticity marginal violation of the original continuous problem is genuine and not due to some round-off error amplification. This situation, which does not lead per se to any particular computational difficulty, is taken here as an opportunity to numerically check the sensitivity of the quoted ellipticity to slight changes in the mesh. A particular mapping is chosen for that purpose. The impact of this option on the ellipticity and on the numerical accuracy of a computed flow is evaluated.

1. Introduction

Chebyshev or Legendre pseudo-spectral methods [1] are of common use for solving the coupled balance equations of momentum, heat and/or mass transfer. Temporal discretization of these equations often leads to elliptic Helmholtz problems. When these multidimensional elliptic problems are separable, their numerical solution can be efficiently obtained using the Successive Diagonalization Technique (SDT), [2,3]. This approach amounts to work in the Helmholtz operator numerical eigenspace, itself being constructed from the tensorial product of eigenspaces of the 1D second derivatives (see [2]). This leads to cheap (for DNS of turbulence, for instance, [4]) and accurate numerical solutions of a large variety of diffusion problems. In particular, each transported quantity has its own set of boundary conditions, possibly different, moreover, in each space direction. A unique 1D coding structure allows us to treat all these boundary conditions. This includes the numerical and computational treatment of the pressure problem, a quasi-Poisson operator [5,6], which does not require any boundary condition to be inverted, as expected since the pressure is known to be often deprived from any boundary condition. In fact the SDT can be implemented in many multidimensional configurations where the differential problem is separable. It works also when there are one or more zero eigenvalues, as in the cases of diffusion problems with Neumann conditions over the whole boundary or of the quasi-Poisson operator for the pressure. It could also work with complex eigenvalues. By the way, the SDT has been extended in [7] to the case where the boundary conditions involve mixed tangential and normal derivatives.

With regard to that, a Galerkin approach [8] for solving these coupled multidimensional elliptic systems does not appear to be as convenient. And there is no way to design a Galerkin formulation to the quasi-Poisson problem. Furthermore the SDT works as well in the physical space so that no back and forth transformation is needed between the physical and spectral spaces.

* Corresponding author. Tel.: +33 1 69 85 81 28.
E-mail addresses: benoit.trouette@limsi.fr, benoit.trouette@gmail.com (B. Trouette), claudine.dang-vu-delcarte@limsi.u-psud.fr (C. Delcarte), gerard.labrosse@u-psud.fr (G. Labrosse).

0021-9991/$ - see front matter © 2010 Elsevier Inc. All rights reserved.
doi:10.1016/j.jcp.2010.06.013

What makes this SDT so easy to implement and so efficient is however the ellipticity of the original continuous problem, provided this ellipticity be preserved at the discrete level. This is obtained in most of the cases, for instance in the Cartesian configuration, viz. with $\frac{\partial^2}{\partial z^2}$ completed with any boundary condition imposed at $z = \pm 1$. In cylindrical coordinates, the easy implementation of the SDT therefore depends upon the ellipticity of the companion operator of $\frac{\partial^2}{\partial z^2}$, namely the polar operator $\left(\frac{1}{r}\frac{\partial}{\partial r}\left(r\frac{\partial}{\partial r}\right) - \frac{k^2}{r^2}\right)$, k being the azimuthal wave number. Polar ellipticity is preserved in its Chebyshev–Gauss–Radau discrete version when a Dirichlet boundary condition is imposed at $r = 1$, say. When Neumann condition is imposed at $r = 1$, a few couples of complex conjugate eigenvalues, with negative real parts, show up for given values of k when the radial cut-off frequency N verifies $N > 13$. This paper shows that the presence of these complex eigenvalues, which marginally violates the ellipticity of the original polar problem, is genuine and not due to some round-off error amplification associated itself with the bad conditioning of the Gauss–Radau matrix.

As said before, the SDT could still be used, remaining efficient, at the expense of an adequate coding of the complex algebra which comes partially into play. Nevertheless it is conceptually interesting to take advantage of this configuration for checking the sensitivity of the ellipticity upon slight changes in the mesh. To this end we have chosen a method, not designed for this purpose, which can continuously stretch the Gauss–Radau grid until making a regular grid. Does a slight change from a Gauss–Radau grid lead back to the ellipticity of the operator? It is observed that this does help for circumventing the occurence of complex eigenvalues. An evaluation is made of the impact this approach has on the accuracy of the solution.

2. Continuous problems

2.1. The inhomogeneous problem

Let us consider the diffusion equation in polar coordinates $(\boldsymbol{e}_r, \boldsymbol{e}_\phi)$,

$$\left(\frac{1}{r}\frac{\partial}{\partial r}\left(r\frac{\partial}{\partial r}\right) + \frac{1}{r^2}\frac{\partial^2}{\partial \phi^2}\right)u = f(r,\phi) \quad \text{with } r \in (0,1) \quad \text{and } \phi \in [0, 2\pi), \tag{1}$$

where $u(r,\phi)$ and $f(r,\phi)$ are real fields. To be quite general a Robin boundary condition is imposed at $r = 1$, viz.

$$au(r=1,\phi) + b\frac{\partial u}{\partial r}(r=1,\phi) = c(\phi) \quad \text{with } \phi \in [0, 2\pi), \tag{2}$$

where the real coefficients a and b are assumed to satisfy the ellipticity sufficient condition, $\frac{a}{b} > 0$. Dirichlet or Neumann conditions respectively correspond to fixing ($b = 0$, $a = 1$) or ($a = 0$, $b = 1$) in (2). All the fields are necessarily periodic in the azimuthal direction. They can therefore be expanded in Fourier series, with

$$\begin{pmatrix} u(r,\phi) \\ f(r,\phi) \\ c(\phi) \end{pmatrix} = \sum_{|k|=0}^{\infty} \begin{pmatrix} \hat{u}_k(r) \\ \hat{f}_k(r) \\ \hat{c}_k \end{pmatrix} e^{ik\phi}, \quad \text{integer } k. \tag{3}$$

Since the left-hand-side fields are real their $k \neq 0$ Fourier components are complex conjugate, $\hat{\bullet}_k(r) = \hat{\bullet}^*_{-k}(r)$, $\bullet = u, f, c$, for $k \neq 0$. Thus, the unknown fields of the expansion (3) are those which correspond to $k \geqslant 0$ for example. Plugging (3) into (1) and (2) leads to the following set of mono-dimensional problems,

$$\left(\frac{1}{r}\frac{\partial}{\partial r}\left(r\frac{\partial}{\partial r}\right) - \frac{k^2}{r^2}\right)\hat{u}_k = \hat{f}_k(r) \quad \text{with } r \in (0,1) \quad \text{and for} \quad k = 0, \ldots, \infty, \tag{4}$$

each completed with a boundary condition, viz.

$$a\hat{u}_k(r=1) + b\frac{d\hat{u}_k}{dr}(r=1) = \hat{c}_k \quad \text{for } k = 0, \ldots, \infty. \tag{5}$$

2.2. The associated homogeneous problems

The associated homogeneous problems read

$$\left(\frac{1}{r}\frac{d}{dr}\left(r\frac{d}{dr}\right) - \frac{k^2}{r^2}\right)u_k = -\lambda^2 u_k; \quad r \in (0,1), \ k = 0, \ldots, \infty, \tag{6}$$

completed with the homogeneous boundary conditions

$$au_k(r=1) + b\frac{du_k}{dr}(r=1) = 0 \quad \text{for } k = 0, \ldots, \infty. \tag{7}$$

The analytical solutions of (6) and (7) express in terms of the Bessel functions of the first kind,

$$u_k(r) = J_k(\lambda r),$$

where λ is any one of the roots, in infinite number, of the following equations,

$$\text{for } k = 0: \ aJ_0(\lambda) = b\lambda J_1(\lambda),$$
$$\text{for } k \geqslant 1: aJ_k(\lambda) + \frac{b}{2}\lambda\big(J_{k-1}(\lambda) - J_{k+1}(\lambda)\big) = 0.$$

All the λ's are real.

3. Discretized problems

3.1. The inhomogeneous problems

Let N be the radial cut-off frequency and r_p, with $p = 0,\ldots,N$, be the radial location of the Chebyshev–Gauss–Radau collocation points, where

$$r_p = \frac{1}{2}\left(1 - \cos\left(\frac{(2p+1)\pi}{2N+1}\right)\right), \quad p = 0,\ldots,N. \tag{8}$$

Choosing the Gauss–Radau nodes allows us to avoid the $r = 0$ singular position which occurs in the operator (4), the closest node to $r = 0$ being at $r_0 = \frac{1}{2}\left(1 - \cos\left(\frac{\pi}{2N+1}\right)\right) \simeq \left(\frac{\pi}{2(2N+1)}\right)^2$. The discrete version of (4) and (5) is obtained by introducing the polynomial approximation of the $\hat{u}_k(r)$'s,

$$\hat{u}_k^{(N)}(r) = \sum_{p=0}^{N} (\hat{u}_k)_p l_p^{(N)}(r) \quad \text{with } (\hat{u}_k)_p \equiv \hat{u}_k^{(N)}(r_p),$$

the $l_p^{(N)}(r)$'s being the Lagrange polynomials based over the Chebyshev–Gauss–Radau nodes (8). Let $\mathbf{D}$ and $\mathbf{D}^{(2)}$ be the respective Gauss–Radau matrix representations of $\frac{d}{dr}$ and $\left(\frac{1}{r}\frac{\partial}{\partial r}\left(r\frac{\partial}{\partial r}\right)\right)$, the superscript (2) indicating that $\mathbf{D}^{(2)}$ is not the square of $\mathbf{D}$. The discretized version of (4) and (5) reads

$$\sum_{q=0}^{N} \mathbf{D}_{pq}^{(2)} (\hat{u}_k)_q - \frac{k^2}{r_p^2}(\hat{u}_k)_p = (\hat{f}_k)_p, \quad p = 0,\ldots,N-1, \quad \text{for} \quad k = 0,\ldots,\infty, \tag{9}$$

where $(\hat{f}_k)_p \equiv \hat{f}_k(r_p)$, and

$$a(\hat{u}_k)_N + b\sum_{q=0}^{N} \mathbf{D}_{Nq}(\hat{u}_k)_q = \hat{c}_k \quad \text{for } k = 0,\ldots,\infty. \tag{10}$$

The matrix system (9) is rectangular. It is made square upon eliminating the $(\hat{u}_k)_N$'s through (10), with

$$(\hat{u}_k)_N = \frac{\hat{c}_k - b\sum_{q=0}^{N-1}\mathbf{D}_{Nq}(\hat{u}_k)_q}{a + b\mathbf{D}_{NN}} \quad \text{for } k = 0,\ldots,\infty.$$

The resulting discrete system reads

$$\sum_{q=0}^{N-1}\left(D_{\underline{R}}^{(2)}\right)_{pq}(\hat{u}_k)_q - \frac{k^2}{r_p^2}(\hat{u}_k)_p = (\hat{f}_k)_p - \frac{\mathbf{D}_{pN}^{(2)}}{a + b\mathbf{D}_{NN}}\hat{c}_k, \quad p = 0,\ldots,N-1, \tag{11}$$

where

$$(D_{\underline{R}}^{(2)})_{pq} = \mathbf{D}_{pq}^{(2)} - \frac{b\mathbf{D}_{pN}^{(2)}\mathbf{D}_{Nq}}{a + b\mathbf{D}_{NN}}. \tag{12}$$

3.2. The homogeneous problems

Implementing the SDT is then based on the eigenmodes of the matrices $\left(D_{\underline{R}}^{(2)} - \frac{k^2}{r^2}\right)$ which come from the l.h.s. of (11), wherein $\frac{k^2}{r^2}$ stands for the diagonal matrix of entries $\frac{k^2}{r_p^2}$, with $p = 0,\ldots,N-1$. Let us therefore introduce the discrete eigenvalue problem,

$$\sum_{q=0}^{N-1}\left(D_{\underline{R}}^{(2)}\right)_{pq}(\widehat{U}_k)_q - \frac{k^2}{r_p^2}\left(\widehat{U}_k\right)_p = \xi(\widehat{U}_k)_p, \quad p = 0,\ldots,N-1 \quad \text{for } k = 0,\ldots,\infty.$$

It leads for each k to N numerical eigenvalues, ξ_n, for $n = 1,\ldots,N$, ordered with increasing absolute value of their real parts.

3.3. The numerical eigenvalues of the polar-diffusion problem

3.3.1. In the Neumann case

For the Cartesian operator, $\frac{d^2}{dx^2} + b.c.$, the numerical eigenvalues can be expressed analytically, [9], whereas, so far, those of $\left(D_{\underline{R}}^{(2)} - \frac{k^2}{r^2}\right)$ can only be obtained by numerical experiments. These latter were performed, for the sake of this analysis, for $N \leqslant 200$ and $k \leqslant 500$. In the Dirichlet case, viz. fixing $a = 1$ and $b = 0$ in (7) and (12), the ξ_n's were found as being all real and negative, $\xi_n = -\lambda_n^2$ with real λ_n's. The situation is fairly different in the Neumann case, $a = 0$ and $b = 1$ in (7) and (12).

Fig. 1 displays the Dirichlet and Neumann numerical spectra obtained with various values of N, all with $k = 4$. The N eigenvalues are all real and negative. As well known, a significant part of them converges towards the analytical spectrum given by the envelope (the analytical zone, say), which is common to all these plots. The remaining part of the numerical spectrum (the numerical zone, say) has a well known specific behavior. But taking now $N = 128$ and $k = 11$ for computing the Neumann spectrum leads to $(N - 2)$ real negative eigenvalues, plus a pair of complex conjugate eigenvalues with real negative parts, while the N Dirichlet ξ_n's remain all real and negative. This is shown in Fig. 2 where $\log_{10}(|Re(\xi_n)|)$ and $\log_{10}(|Im(\xi_n)|)$ are plotted as functions of $\log_{10}(n)$. The pair of complex conjugate eigenvalues occur at the end of the analytical zone, with a real part falling at the right location. Both (equal) imaginary parts are small, but definitely not compatible with the machine zero. The lowest $k(N)$ value which leads to complex eigenvalues of $\left(D_{\underline{R}}^{(2)} - \frac{k^2}{r^2}\right)$ has been looked for. The result is given in Fig. 3: there is at least one particular value of k, $k \leqslant 500$, for most of the values taken by N, for $N \geqslant 13$, where complex eigenvalues occur in the Neumann spectrum.

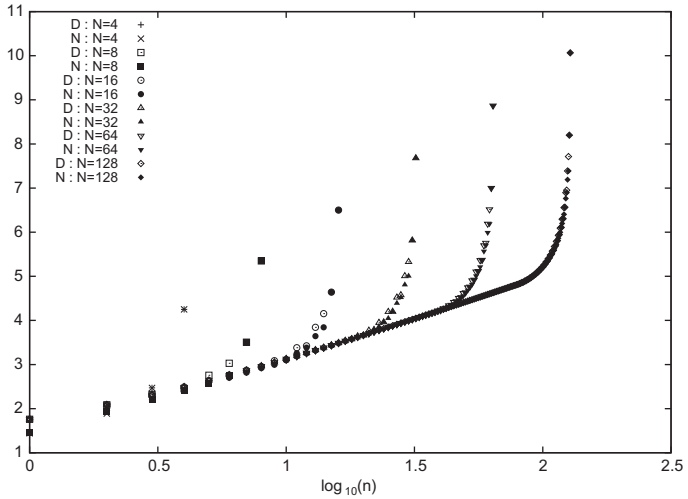

Fig. 1. $\log_{10}(|\xi_n|)$ as a function of $\log_{10}(n)$, $n = 1,\ldots,N$, for the Dirichlet (D) and Neumann (N) cases, obtained with various N's and $k = 4$.

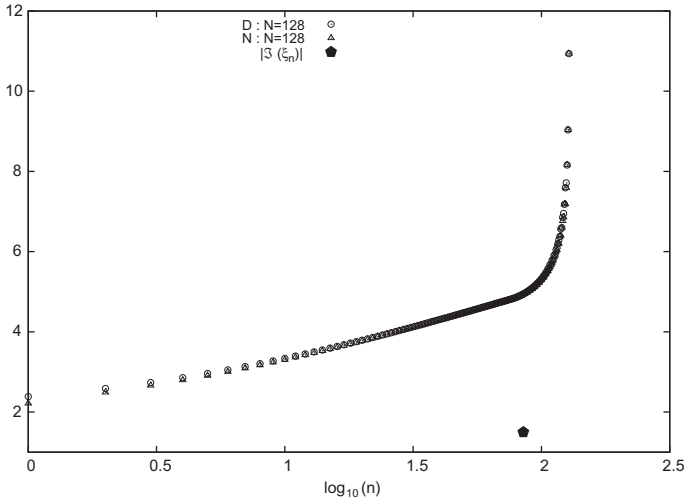

Fig. 2. $\log_{10}(|Re(\xi_n)|)$ and $\log_{10}(|Im(\xi_n)|)$ as functions of $\log_{10}(n)$, $n = 1,\ldots,N$, for the Dirichlet (D) and Neumann (N) cases, obtained with $N = 128$ and $k = 11$.

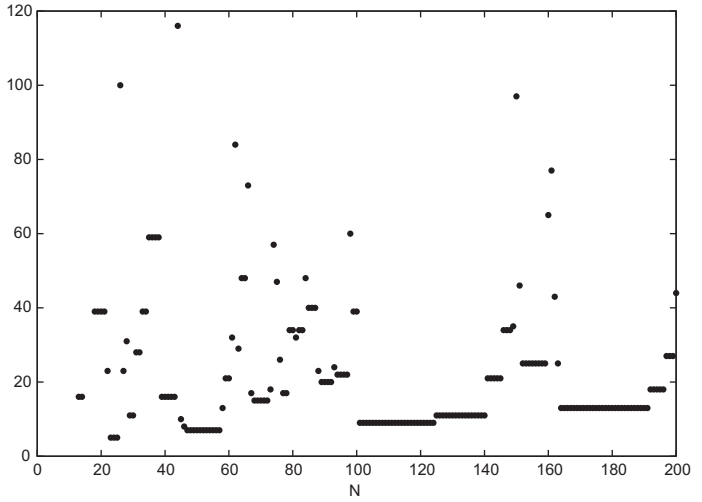

Fig. 3. The lowest $k(N)$ values which lead to complex eigenvalues of $\left(D_{\underline{R}}^{(2)} - \frac{k^2}{r^2}\right)$.

3.3.2. In the Robin case

When the Robin conditions (5) are adopted, and discretized using a Gauss–Radau grid with $N+1$ nodes, the order of magnitude of the Neumann contribution is $|b|N^2$. It is therefore expected that complex eigenvalues will occur in the polar-diffusion problem if $|b|N^2 \gg |a|$.

3.4. Origin of the numerical complex eigenvalues

Should these complex eigenvalues be considered as spurious, and/or simply due to the bad conditioning of the matrix $\left(D_{\underline{R}}^{(2)} - \frac{k^2}{r^2}\right)$? The answer is supplied by two numerical tests, both performed with $k = 39$. As indicated by Fig. 3, complex eigenvalues occur with $N = 18, 19, 20, 21$ for example. First, computing them for $N = 20$ while increasing the number of significant digits, as it is made possible by the Mathematica software, shows that the complex eigenvalues are not sensitive to round-off errors. They definitely converge to more and more accurately determined values, $-11879.8 \pm 17.3509i$, or so. Second, computing the eigenvalues for $N = 22$, now, leads to a purely real spectrum, despite the fact that the matrix conditioning should be worst than with $N = 20$. It can thus be concluded that the complex eigenvalues are genuine eigenvalues of the discrete problem.

4. Is the ellipticity sensitive to slight changes of the grid?

4.1. Introduction

The Gauss grids (including the Gauss–Radau and Gauss–Lobatto cases) are known to be required for satisfying two intimately related criteria. First, they give access to the most accurate polynomial interpolation, in a bounded region, of any continuous function. Second, they preserve in the discrete space the orthogonality relations between the polynomials of the basis defined in the continuous realm. Should these grids preserve the ellipticity of the continuous operator? The answer is positive in most of the cases. However, it has been observed that the Projection–Diffusion uncoupling of the velocity and pressure, the consistent Stokes solver analysed in [6], presents a few couples of complex conjugate eigenvalues when Dirichlet boundary conditions are imposed on the velocity. This marginal violation of the Stokes ellipticity looks like the one this paper is devoted to since, in both cases, the discrete operator mixes parts of second and first derivative matrices, the first derivative coming from $\mathbf{V}p$ in the Stokes solver and from the Neumann condition in the present problem.

Let us see therefore if the ellipticity can be recovered by making slight changes in the Gauss–Radau grid.

4.2. The mapping

To this end, we will use a mapping proposed in [10] by Kosloff and Tal-Ezer. Their goal is to increase, from an $\mathcal{O}(N^{-2})$ to an $\mathcal{O}(N^{-1})$ limitation, the CFL critical time step value that occurs when solving the 1D hyperbolic equation, on a Gauss–Lobatto grid. This mapping will thus move our Gauss–Radau nodes of abscissae r_i to new locations of abscissae x_i, according to the α-mapping relation

$$x_i = g(r_i;\alpha) = \frac{\arcsin(\alpha r_i)}{\arcsin(\alpha)} \in (-1,1] \quad \text{for} \quad i = 0,\ldots,N \quad \text{with} \quad 0 \leqslant \alpha < 1.$$

For α going until 0.9, or so, the mapping just slightly moves the Gauss–Radau nodes, keeping the $\mathcal{O}(N^{-2})$ refinement at both extremities of the radial axis, while values of α very close to 1 lead to almost evenly distributed nodes over $(-1,1]$.

This mapping has been widely studied (see the review by Boyd [11] p. 335, and more recent contributions, for example [12]). All these analyses are focussed onto finding the value of the mapping parameter α which both increases the critical time step of a CFL stability criterion and preserves the spectral accuracy of the results. We now use this mapping for an elliptic problem, and with a different goal. We just hope to, at least, delay in N and k the occurrence of complex eigenvalues while not losing a significant level of accuracy. According to some of the quoted analyses (Hesthaven et al. [13] and Boyd [11]), and taking into account the fact that we use a not too large range of N values (somewhere in between 30 and 160), we choose $\alpha = 0.9$. This value is not too far from the value $\alpha = \cos(1/2) \simeq 0.87$ suggested by [11]. As a matter of comparison, 0.99-mapping is also considered.

We will see if ellipticity is recovered and evaluate the impact this option has on the numerical accuracy of a flow simulation.

4.3. Mapping of the derivation operators

Any function $f(r)$ is transformed into $h(x)$ whose first derivative is obtained from

$$\frac{dh}{dx} = \frac{1}{g'(r;\alpha)}\frac{df}{dr} \quad \text{with } g'(r;\alpha) = \frac{\partial g}{\partial r}.$$

The radial discrete first derivative $\mathbf{D}$ is transformed as

$$\mathbf{D} \to \mathbf{A}\cdot\mathbf{D},$$

where $\mathbf{A}$ is a diagonal matrix whose entries are given by

$$\mathbf{A}_{ii} = \frac{1}{g'(r_i,\alpha)}, \quad i = 0,\ldots,N,$$

where

$$g'(r_i;\alpha) = \frac{\alpha}{\arcsin(\alpha)\sqrt{1-(\alpha r_i)^2}},$$

In the same way, the matrix $\mathbf{D^2}$ which represents $\frac{d^2}{dr^2}$ is modified according to

$$\mathbf{D^2} \to \mathbf{A}^2\cdot\mathbf{D^2} + \mathbf{B}\cdot\mathbf{D},$$

the diagonal matrix $\mathbf{B}$ being defined by

$$\mathbf{B}_{ii} = -\frac{g''(r_i;\alpha)}{[g'(r_i;\alpha)]^3}, \quad i = 0,\ldots,N,$$

where

$$g''(r_i;\alpha) = \frac{\alpha^3}{\arcsin(\alpha)}\cdot\frac{r_i}{[1-(\alpha r_i)^2]^{3/2}}.$$

4.4. Impact on the ellipticity of the polar-diffusion operator

Figs. 4 and 5 show the way the $k(N)$ configuration which leads to complex eigenvalues has been modified with these 0.9- and 0.99-mappings, comparing them with Fig. 3. Complex eigenvalues are still occurring, but for higher values of N, viz. $N \geqslant 29$ and $N \geqslant 81$ respectively, and also for much larger values of k.

4.5. Mapping and accuracy: comparison on a physical configuration

It is instructive to evaluate the accuracy impact of the mapping in a practical case. We now consider the axi-symmetric floating-zone problem in microgravity environment which is described in detail in [14,15]. A cylindrical liquid bridge, of height $2H$ and radius R, is maintained by surface tension between two horizontal isothermal solid disks. Its lateral free surface is submitted to a steady and parabolic heat flux. This triggers and maintains a thermocapillary flow: the surface tension variations, due to the thermal gradients on the free surface, generate tangential stresses and then viscous driving of the liquid. The flow is generally studied in a two-parameter space: the Prandtl number (Pr), ratio between momentum and thermal diffusivities, and the Marangoni number (Ma), ratio between thermocapillary and thermal diffusion velocities. The axi-symmetric velocity and temperature fields of the flow were deeply studied on a large domain of the parameter space in

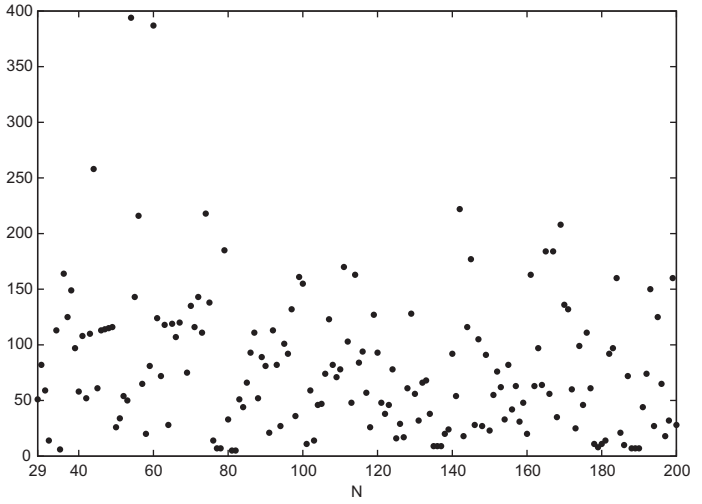

Fig. 4. The lowest $k(N)$ values leading to complex eigenvalues of $\left(D^{(2)}_{\underline{R}} - \frac{k^2}{r^2}\right)$, with $\alpha = 0.9$.

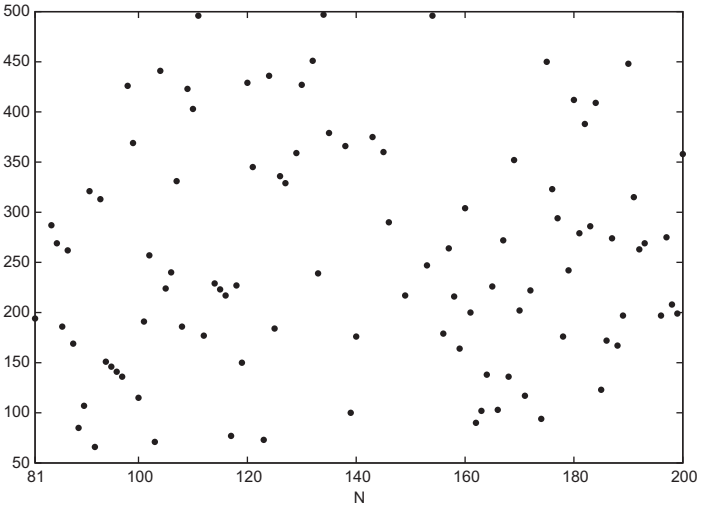

Fig. 5. The lowest $k(N)$ values leading to complex eigenvalues of $\left(D^{(2)}_{\underline{R}} - \frac{k^2}{r^2}\right)$, with $\alpha = 0.99$.

[14,15]. The impact of the numerical treatment of the vorticity singularity which occurs at the junction of the free surface with the rigid disks was explored in [16,17]. The governing equations are given in Appendix A.

Let w_{ij} be the set of the axial-velocity nodal values obtained on the Gauss–Radau grid, and w^{map}_{ij} the corresponding set obtained from the 0.9-mapping applied on this grid. A Gauss–Lobatto grid is used in the axial direction.

Fig. 6 presents two sets of different data. The iso-w lines are plotted in both left panels, with 70 and 100 as cut-off values in the radial and axial directions. The upper right panel shows the relative difference

$$E_{ij} = \frac{|w^{map}_{ij} - w_{ij}|}{\max_{i,j}|w^{map}_{ij}|}, \tag{13}$$

computed over the mapped grid. The associated scale in this figure indicates that this relative error stays around the value 10^{-7}. Taking now $\alpha = 0.99$, the relative error E is then amplified by three decades. The relative difference between the 0.9-mapped and unmapped results is thus not too important. The grid transformation can therefore be used to stay in an elliptic context.

4.6. Impact of the mapping on the polar-diffusion spectrum

The maximum discrepancy is observed in Fig. 6 to be located in regions of steep vorticity gradient, which corresponds to high spatial frequencies of the solution. This section shows the reason of this behavior.

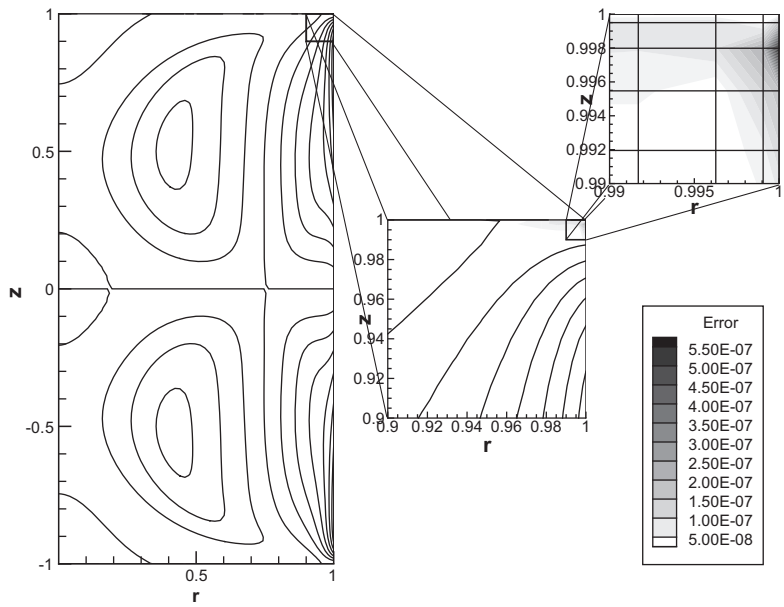

Fig. 6. Iso-w lines in the two leftmost panels, and, in the right panels, the relative difference $E_{ij} = \frac{|w_{ij}^{map} - w_{ij}|}{\max_{i,j}|w_{ij}^{map}|}$, with its scale, for $\alpha = 0.9$ ($Ma = 106$ and $Pr = 0.01$).

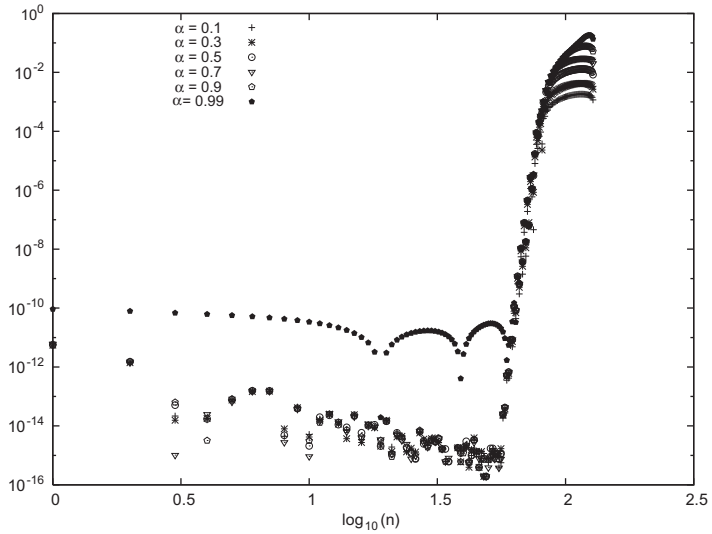

Fig. 7. Relative differences $\left|\frac{\xi_n^{(\alpha)} - \xi_n}{\xi_n}\right|$, for a Neumann case, with $N = 128$ and $k = 4$ obtained from several values of α.

Thanks to the mapping, spectra which were previously polluted by complex eigenvalues are now purely real. But does this mapping affect, and to which extent, the spectrum itself of the polar-diffusion operator? Let $\xi^{(\alpha)}$ be the set of the numerical eigenvalues of this operator obtained from an α-mapping. We compare it with the ξ's obtained without mapping. One of the Neumann cases presented in Fig. 1 is chosen. It corresponds to $N = 128$, $k = 4$. In Fig. 7 are plotted the relative differences $\left|\frac{\xi_n^{(\alpha)} - \xi_n}{\xi_n}\right|$ obtained for several values of α. Two regions clearly show up. The first region is the part of the spectra where the numerical eigenvalues are in good agreement with the analytical ones, the common envelope in Fig. 1. The mapping significantly affects the accuracy of these numerical eigenvalues, but at a level which is without any practical importance. The second region lies in the purely numerical part of Fig. 1, wherein the eigenvalues strongly depart from the analytical ones. This is the region of Fig. 7 which exhibits a very steep increase of the relative differences. The practical consequences of this behavior in Fig. 7 are precisely exhibited in the upper right panel of Fig. 6.

5. Conclusion

The Chebychev Gauss–Radau discrete version of the polar-diffusion operator, associated with a Neumann boundary condition at $r = 1$, does not preserve the expected ellipticity. Numerical complex conjugate eigenvalues, with negative real parts, are indeed obtained for a set of values of both the azimuthal wave number k and the Gauss–Radau cut-off frequency N. We have shown that these complex eigenvalues are genuine eigenvalues of the discrete version of this operator. Adopting a slight transformation of the Gauss–Radau grid which preserves the $\mathcal{O}(N^{-2})$ refinement at both extremities of the radial axis, delays in N and k the occurence of these complex eigenvalues. This clearly indicates that the discrete ellipticity is very sensitive to the location of the nodes in the grid. The effective departure between a numerical flow obtained in this way and the corresponding Gauss–Radau solution has been observed as globally small. The only zone in the flow where significant discrepancies appear is where a strong gradient occurs. This is related to the impact the mapping has on the polar operator numerical spectrum. It is indeed important for the high space-frequency eigenvectors.

Appendix A. Governing equations for the thermocapillary problem

The axi-symmetric physical problem is governed by the following non-dimensional Navier–Stokes and energy equations, in the Boussinesq approximation framework,

$$\frac{\partial \boldsymbol{u}}{\partial t} + (\boldsymbol{u}\cdot\boldsymbol{\nabla})\boldsymbol{u} = -\boldsymbol{\nabla} p + Pr\left(\boldsymbol{\nabla}^2 - \frac{\boldsymbol{e}_r}{r^2}\right)\boldsymbol{u}, \tag{14}$$

$$\frac{\partial \theta}{\partial t} + (\boldsymbol{u}\cdot\boldsymbol{\nabla})\theta = \boldsymbol{\nabla}^2\theta, \tag{15}$$

$$\boldsymbol{\nabla}\cdot\boldsymbol{u} = 0, \tag{16}$$

where $\boldsymbol{u}$, θ and p, respectively are the non-dimensional velocity, temperature and pressure. The unit vectors $\boldsymbol{e}_r$ and $\boldsymbol{e}_z$ define respectively the radial and axial directions, their origin being located at the center of the liquid bridge (center of the cylinder). The operators are defined as follows: $\boldsymbol{\nabla} = \boldsymbol{e}_r(\partial/\partial r) + \boldsymbol{e}_z(\partial/\partial z), \boldsymbol{\nabla}^2 = (1/r)(\partial/\partial r)[(r(\partial/\partial r))] + \partial^2/\partial z^2$. Noting $\boldsymbol{u} = v\boldsymbol{e}_r + w\boldsymbol{e}_z$, one has also $\boldsymbol{\nabla}\cdot\boldsymbol{u} = (1/r)[\partial(rv)/\partial r] + (\partial w/\partial z)$ and $\boldsymbol{u}\cdot\boldsymbol{\nabla} = v(\partial/\partial r) + w(\partial/\partial z)$.

To complete the set (14)–(16), boundary conditions are specified:

$$\begin{cases} \bullet\ z = \pm 1 \begin{cases} \boldsymbol{u} = \boldsymbol{0} \text{ (no-slip conditions)}, \\ \theta = 0 \text{ (imposed temperature)}, \end{cases} \\ \bullet\ r = 1 \begin{cases} v = 0 \text{ (non-deformable free surface)}, \\ \frac{\partial w}{\partial r} = -Ma\frac{\partial \theta}{\partial z} f(z) \text{ (stress condition)}, \\ \frac{\partial \theta}{\partial r} = q(z) \text{ (heat flux)}. \end{cases} \end{cases} \tag{17}$$

with $q(z) = (1 - z^2)^2$ the heat flux. The parameter values are $Pr = 0.01$ and $Ma = 106$. The function $f(z) = (1 - z^{2n})^2$ is introduced for regularizing the vorticity singularity, n being here fixed to 13 according to the results of [16,17].

The system (14)–(16) is space-discretized with a Chebyshev collocation method based on radial Gauss–Radau and axial Gauss–Lobatto grids. Uncoupling the velocity and pressure fields is made with the Projection-Diffusion method, [5,6]. Time integration is performed with an usual second order finite difference scheme.

References

[1] C. Canuto, M. Hussaini, A. Quarteroni, T. Zang, Spectral Methods in Fluid Dynamics, Springer Series in Computational Physics, Spectral Methods in Fluid Dynamics, Springer Series in Computational Physics, Springer-Verlag, New York, 1988.
[2] P. Haldenwang, G. Labrosse, S. Abboudi, M. Deville, Chebyshev 3D Spectral and 2D pseudospectral solvers for the Helmholtz equation, J. Comput. Phys. 55 (1984) 115–128.
[3] R. Lynch, J. Rich, D. Thomas, Direct solution of partial differential equations by tensor product methods, Numer. Math. 6 (1964) 185–199.
[4] E. Leriche, S. Gavrilakis, Direct numerical simulation of the flow in a lid-driven cubical cavity, Phys. Fluids 12 (6) (2000) 1363–1376.
[5] A. Batoul, H. Khallouf, G. Labrosse, Une Méthode de Résolution Directe (Pseudo-Spectrale) du Problème de Stokes 2D/3D Instationnaire. Application à la Cavité Entrainée Carrée, C. R. Acad. Sci. Paris 319 (I) (1994) 1455–1461.
[6] E. Leriche, G. Labrosse, High-order direct Stokes solvers with or without temporal splitting: numerical investigations of their comparative properties, SIAM J. Sci. Comput. 22 (4) (2000) 1386–1410.
[7] S. Nguyen, C. Delcarte, A spectral collocation method to solve Helmoltz problems with boundary conditions involving mixed tangential and normal derivatives, J. Comput. Phys. 200 (2004) 34–49.
[8] J. Shen, Efficient spectral-Galerkin method II. Direct solvers of second and fourth order equations by using Chebyshev polynomials, SIAM J. Sci. Comput. 16 (1) (1995) 74–87.
[9] H. Vandeven, On the eigenvalues of second-order spectral differentiation operators, Comput. Methods Appl. Mech. Eng. 80 (1990) 313–318.
[10] D. Kosloff, H. Tal-Ezer, A modified Chebyshev pseudospectral method with an $O(N^{-1})$ time step restriction, J. Comput. Phys. 104 (1993) 457–469.
[11] J. Boyd, Chebyshev and Fourier spectral methods, Dover Publishers, New York, 2001.
[12] J. Mead, R. Renaut, Accuracy, resolution, and stability properties of a modified Chebyshev method, Siam J. Sci. Comput. 24 (2002) 143–160.
[13] J. Hesthaven, P. Dinesen, J. Lynov, Spectral collocation time-domain modeling of diffractive optical elements, J. Comput. Phys. 155 (1999) 287–306.
[14] E. Chénier, C. Delcarte, G. Labrosse, Stability of the axisymmetric buoyant-capillary flows in a laterally heated liquid bridge, Phys. Fluids 11 (3) (1999) 527–541.

[15] E. Chénier, C. Delcarte, G. Kasperski, G. Labrosse, Sensitivity of the liquid bridge hydrodynamics to local capillary contributions, Phys. Fluids 14 (9) (2002) 3109–3117.
[16] G. Kasperski, G. Labrosse, On the numerical treatment of viscous singularity in wall-confined thermocapillary convection, Phys. Fluids 12 (11) (2000) 2695–2697.
[17] E. Chénier, C. Delcarte, G. Kasperski, G. Labrosse, Thermocapillary flows and vorticity singularity, in: R. Narayanan, D. Schwabe (Eds.), Interfacial Fluid Dynamics and Transport Process, Lecture Notes in Physics, vol. 628, Springer-Verlag, Berlin, Heidelberg, New York, 2003.